## PAPER

Check for updates

# Facile synthesis of the SnTe/SnSe binary nanocomposite *via* a hydrothermal route for flexible solid–state supercapacitors†

Muhammad Abdullah,[a] Peter John,*[a] Khaled Fahmi Fawy,[b] Sumaira Manzoor,[c] Kashif Younas Butt,[d] Abdul Ghafoor Abid,[c] Mouslim Messali,[e] Muhammad Najam-Ul-Haq [ID][c] and Muhammad Naeem Ashiq [ID] *[c]

Environmental degradation and energy shortage are the two biggest problems facing the world right now. Because of the limited supply of non-renewable sources, the production of environment-friendly energy and its storage has gained significant importance. Pseudocapacitors have lately caught the interest of energy specialists due to their greater energy/power density and prolonged cycle life. In this work, binding-free SnTe/SnSe (STSS) electrodes deposited onto Ni foam (NF) as the conductive substrate have been developed by a facile hydrothermal route for supercapacitor applications. Several analytical tools were utilized to study the morphological, structural and textural characteristics. The electrochemical results obtained from a three-electrode system suggest that the STSS electrode material exhibits great specific capacitance ($C_s$) of 1276 F g$^{-1}$, specific energy ($E_d$) of 46.45 W h kg$^{-1}$ and specific power ($P_d$) of 256 W kg$^{-1}$ @ 1 A g$^{-1}$. The results of $C_{dl}$ indicate that the STSS (31.28 mF) has a larger $C_{dl}$ value than those of SnTe (23.22 mF) and SnSe (26.35 mF). The analysis of electrochemical stability indicates that the STSS displays structural stability over 5000 cycles with a maximum capacitance retention of 96%. The Nyquist plot profile displayed a smaller $R_{ct}$ value for STSS (0.89 Ω) than SnSe (1.13 Ω) and SnTe (1.97 Ω). The symmetric behavior of STSS was determined in 2.0 M potassium hydroxide. The results reveal that this material has a specific capacitance of 537.72 F g$^{-1}$ and specific energy of 78.32 W h kg$^{-1}$. These findings suggest that the STSS electrode might serve as a potential candidate for supercapacitors and other energy-saving equipment.

## 1. Introduction

Recently, the world has been consuming energy rapidly, while not enough is being produced; thus there is need for clean and reproducible energy resources. Consequently, one of the most challenging elements of energy technology research is the development of highly efficient ways of transforming and storing energy.[1] The supercapacitor is a novel energy storage technology that stands out among conventional capacitors and lithium-ion batteries. However, the supercapacitor displays exceptional power density ($P_d$) and energy density ($E_d$) more than batteries and fuel cells. Therefore, supercapacitors have

a positive future in the market as energy storage devices, and their application is expanding by the day.[2–4] Both double-layer electrochemical capacitors and pseudocapacitors store energy *via* reversible and rapid faradaic redox reactions on the surface of electrocatalytic species, and electrochemical double-layer capacitors (EDLCs) typically give an elevated $P_d$ (10k W kg$^{-1}$) and exhibit exceptional cycling characteristics ($10^4$ cycles).[5,6] Thus, faradaic pseudocapacitors have more specific capacitance and specific energy than conventional capacitors (100 W h kg$^{-1}$). In comparison, pseudocapacitors have parts that store both chemical and physical energy. EDLCs completely rely on the physical storage of energy. Pseudocapacitors exhibit several advantages over EDLCs, including higher power density, significantly longer lifetimes, and enhanced energy density, as they allow energy storage within the bulk of the electrode materials and at their surface.[7,8] Because supercapacitors store less energy than standard batteries, they cannot be utilized as frequently. Therefore, scientists are trying to develop electrode materials *i.e.* composites with other transition metal chalcogenides to boost the energy density ($E_d$) of supercapacitors.[9,10] Generating new nanostructured materials with greater electrode porosity and interfacial area can boost the specific

[a]Department of Chemistry, Government College University, Lahore, Pakistan

[b]Department of Chemistry, Faculty of Science, King Khalid University, P.O. Box 9004, Abha 61413, Saudi Arabia

[c]Institute of Chemical Sciences, Bahauddin Zakariya University, Multan, 60800, Pakistan. E-mail: naeembzu@bzu.edu.pk

[d]Department of Chemistry, University of Lahore, Lahore, Pakistan

[e]Department of Chemistry, College of Science, Imam Mohammad Ibn Saud Islamic University, P.O. Box, 90950, Riyadh 11623, Saudi Arabia

capacitance ($C_s$). In a similar vein, expanding the useable voltage range can be achieved by modifying the electrolyte (organic, ionic, aqueous or redox-added electrolytes) and electrode fabrication (asymmetric or symmetric).[11]

Ruthenium oxide ($RuO_2$) is a prominent transition metal oxide used in pseudocapacitor electrodes because of its unique properties; however, due to its high cost, its commercial utilization is difficult and severely confined. In recent years, numerous transition-metal oxides like $MnO_2$,[12] $NiO_x$,[13] $Co_3O_4$,[14] and $PbO_4$,[15] in addition to oxide materials, conducting polymers[16] and carbonaceous material,[17] have been studied as supercapacitor electrode materials to enhance the electrochemical performance. Tin (Sn), an n-type semiconductor, has a good electrochemical capacitive property. The unique electrical and conductive properties of tin oxide have garnered a lot of attention as it can be used in a variety of applications. Electrode materials, catalysts, gas monitors, electrochromic devices, and dye-based solar cells are a few of its many fields of application.[18] It has been demonstrated that metal selenides[19] and tellurides[20] are two of the most important chalcogenide compounds that possess remarkable electrochemical properties. Metallic Te-based electrodes have received less attention than other transition metal chalcogenide materials for their pseudocapacitive properties and less cycling stability. However, due to its superior electrical properties, metallic Se is frequently used as a working electrode in power storage devices. Se-based electrode materials have excellent charge and ion kinetics, as well as short diffusion paths. Mixing carbon, metal oxides and hydroxides to form a composite with these materials results in high specific capacitance of the resultant electrode materials. Significant progress has been made in the creation of composites composed of two pseudocapacitance materials.[21] Transition metal selenides (TMSs) have been suggested as potential electrocatalytic materials for electrochemical energy saving equipment due to their synergistic interface with many metallic ions, which may greatly improve the electrochemical properties, such as the redox-active region, power density, cycling stability and specific energy. The rate capacity and energy density of TMSs may be higher than those of the sulfides and oxides of the same elements.[11] The electrochemical characteristics of pure tin-selenide and tin telluride do not fulfil the industry standards because of the low cycling stability. Therefore, many methods are employed to improve the functionality of these electrode materials, such as morphology control, composite manufacturing and elemental doping.

Several researchers have reported Te- and Se-based electrodes for supercapacitor applications. B. Pandit et al. industrialized the SnSe nanosheet for energy storage application via a colloidal method. The generated electrode material exhibited a $C_s$ of 619.7 F g$^{-1}$ and high $E_d$ of 28.5 W h kg$^{-1}$ @ 2 mV s$^{-1}$ sweeping speed.[22] Ahmed et al. fabricated the SnSe/rGO nanocomposite via a solvothermal process for application in energy storage equipment. The SnSe/rGO-based compound revealed a $C_s$ of 568 F g$^{-1}$, $P_d$ of 1.007 kW kg$^{-1}$, and $E_d$ of 30.5 W h kg$^{-1}$ @ 1 A g$^{-1}$.[23] Dan Ni and coworkers developed a SnSe electrode material to build a supercapacitor device with the $C_s$ of 214.4 F g$^{-1}$ and 182.8 F g$^{-1}$ respectively at 1 A g$^{-1}$ and 20 A g$^{-1}$.[24] B. Ye

et al. synthesized NiSe/ZnSe for asymmetric capacitors via electrodeposition. The electrode material showed a high $C_s$ of 651.5 mA h g$^{-1}$ at 1 A g$^{-1}$ and 97.6% retention capacitance.[25] B. Ye et al. described the fusion of the NiSe/NiTe complex for energy storage systems via a hydrothermal strategy. The electrode material showed a high $C_s$ of 1868 F g$^{-1}$ with an $E_d$ of 33.7 W h kg$^{-1}$ at 1 A g$^{-1}$.[26]

In addition, a significant number of studies have been carried out on a wide range of feasible composite fabrication methods that can affect the electrochemical features of the electrocatalytic materials, including electrodeposition, hydrothermal method, coprecipitation, and sol–gel approach. These can be employed to produce transition-metal chalcogenide nanocomposites. Among other methods, the hydrothermal method is preferred as it provides control over the crystal size, morphology, high purity and versatility and is an energy-efficient process.[27] A. M. Zardkhoshoui et al. developed the $NiGa_2S_4$-rGO pseudocapacitive electrode material via a hydrothermal method, and it possessed a $C_s$ of 2124 F g$^{-1}$ with a 73% retention of capacitance.[28] S. Arunpandiyan et al. fabricated the ZnO/NiO:rGO nanocomposite through a hydrothermal route and demonstrated a $C_s$ of 622.3 F g$^{-1}$ in 1 M potassium hydroxide.[29] Y. Tian et al. produced nickel selenide nanorods via a hydrothermal approach for supercapacitor application. The capacitance of the NiSe material was 6.81 F g$^{-1}$ @ 5 mA cm$^{-2}$.[30] Jiahong Zheng et al. created $NiSe_2$/$MoS_2$/CQDs with a $C_s$ of 1540.7 F g$^{-1}$ and 80.6% rate capability at 20 A g$^{-1}$ over 2000 cycles for supercapacitor application.[31]

Inspired by the excellent electrochemical properties of these metal chalcogenides (Se and Te), we prepared a self-supporting SnTe/SnSe composite nanostructure via a hydrothermal strategy for supercapacitor equipment. Several analytical approaches were used to measure the morphological, structural and textural aspects of the generated electrode material. When used as the electrode. SnTe/SnSe demonstrated outstanding electrocatalytic activity with a $C_s$ of 1276 F g$^{-1}$ @ 1 A g$^{-1}$ and capacitance retention of 96% over 5000 cycles because of their complementary redox activity. Its high capacitive performance is related to increased electrical conductivity and electrolyte wettability, faster electron dispersion, and unimpeded ion transit. Therefore, this work not only demonstrates the importance of transition metal chalcogenides but also provides a new path for energy storage appliances.

## 2. Experimental section

### 2.1. Reagents

Tin chloride ($SnCl_2$, Sigma Aldrich, 99%), tellurium powder (Merck, 99%), potassium hydroxide (KOH, Sigma Aldrich, >85%), selenium powder (Se, Sigma Aldrich, 99%), hydrochloric acid (HCl, AnalaR, 37%), absolute ethanol ($C_2H_5OH$, Sigma Aldrich, >98%) and distilled deionized water (DI, $H_2O$) were employed as such in the fabrication of SnTe/SnSe without any processing.

### 2.2. Fabrication of the SnTe nanostructures

For the manufacturing of tin telluride, 0.1 M of Te powder was mixed in 50.00 mL of DI $H_2O$ under continuous mixing for
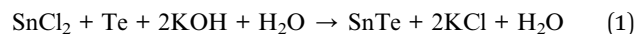
40 min to make a homogeneous solution. Following that, 10 mL of the 6 M potassium hydroxide solution was gradually added drop by drop under continuous stirring, and then, 5.00 mL of hydrazine monohydrate was poured into the reaction mixture under vigorous magnetic stirring on a magnetic hotplate. 0.1 M of tin chloride was added to the resultant mixture after 20 min of vigorous mixing. Lastly, the obtained product was poured into the autoclave and kept in an electric furnace for 12 h at 170 °C. The solution suspension was thoroughly rinsed many times with absolute ethanol and DI $H_2O$ before being heated at 60 °C for 12 hours. The dehydrated end material was ground and stored in plastic vials to avoid exposure to the atmospheric moisture content and used for the fabrication of other composites.

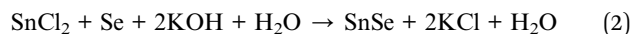### 2.3. The synthesis of SnSe and the SnTe/SnSe nanocomposite

In the typical synthesis of the SnTe/SnSe nanocomposite, 0.1 M Se powder was mixed in deionized water under constant agitation along with the dropwise addition of 10 mL of 6.0 M aqueous solution of KOH (potassium hydroxide), followed by the addition of 5 mL of $N_2H_4$. Next, 0.5 g of already synthesized SnTe was added to the above mixture. After constant agitation, the resulting material was transformed into an autoclave and placed in a muffle dehydrator (oven) at 170 °C for 12 h. The resultant products were separated using centrifugation, rinsed with $C_2H_5OH$ and DI $H_2O$, dried in an electric furnace at 60 °C for 12 h and then, allowed to cool to ambient temperature. For comparison, pristine SnSe was also prepared by the aforementioned method under the same condition without the addition of SnTe. The chemical processes that take place during fabrication are given below as expressions 1 and 2, and the graphical representation of the synthesis of the SnTe/SnSe nanocomposite is given in Scheme 1.

For SnTe

$$SnCl_2 + Te + 2KOH + H_2O \rightarrow SnTe + 2KCl + H_2O \quad (1)$$

For SnSe

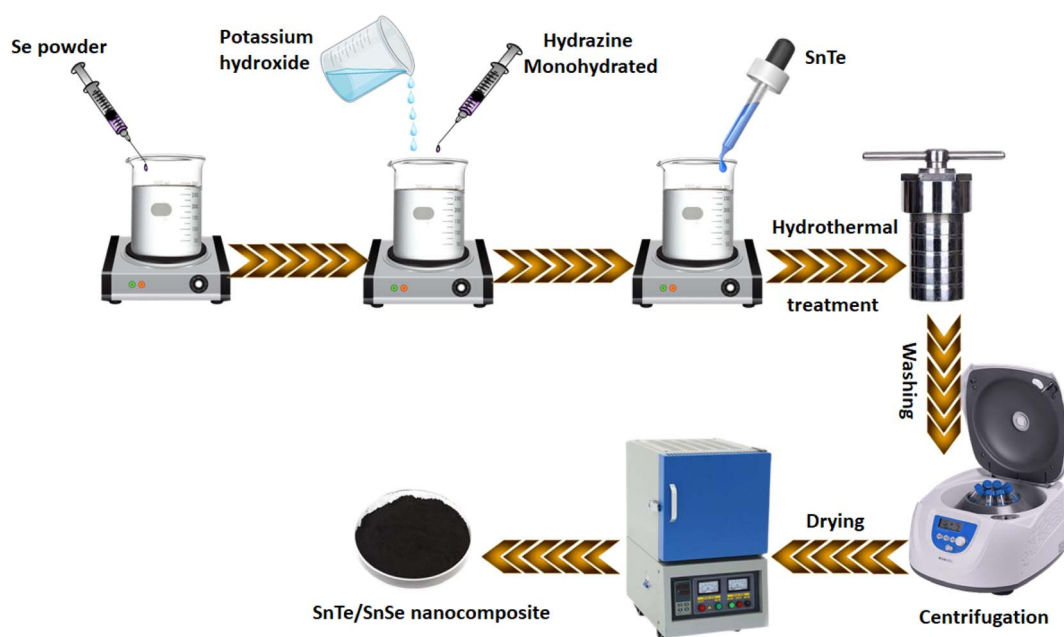$$SnCl_2 + Se + 2KOH + H_2O \rightarrow SnSe + 2KCl + H_2O \quad (2)$$

### 2.4. Instrumental analysis

The crystallographic parameters of the fabricated electrode substances were evaluated by powder X-ray diffraction (PXRD, Advance D8 Bruker) using nickel-filtered copper-Kα radiation exhibiting a $\lambda$ of 1.5418 Å. Furthermore, the structural features of the material were determined by Fourier transform infrared spectroscopy (FTIR, JASCO-6800) in the range of 400 to 4000 cm$^{-1}$. The surface features and elemental makeup of the product were characterized by scanning electron microscopy coupled with energy-dispersive X-ray diffraction (SEM-EDX, Quanta 200-FEG). The textural features of the synthesized product were determined by the Brunauer–Emmett–Teller method (BET, Nova2200e Quantachrome) through $N_2$ sorption adsorption/desorption studies. The elemental makeup and valence states of the fabricated product were investigated by X-ray photoelectron spectroscopy (XPS) using a PHI 5000.

### 2.5. Electrode assembly

Firstly, the Ni foam (NF) was rinsed with acetone, absolute $C_2H_5OH$ and deionized $H_2O$. After that, the NF was dehydrated in an oven at 60 °C, and the electrocatalytic mixture was put



**Scheme 1** Schematic representation of the fabrication of the SnTe/SnSe nanocomposite.

together by combining 0.005 g of the synthesized product in 75 µL of deionized $H_2O$ as the solvent. The electrocatalytic ink was cast on nickel foam by the drop-casting strategy and then put in an electric furnace at 40 °C for 2 h. All the working electro-catalysts were manufactured by following the same method, and their electrical performances were measured under ambient conditions. The electrochemical Pyrex cell was also rinsed with aqua regia to remove impurities from the Pyrex glass walls.

## 2.6. Electrical characterization

The electrical activity of the binder-free electrode material was investigated with a Meterohm autolab (PG STAT-204) equipped with a 3-electrode system. The working electrode material (0.005 g) was developed on Ni foam, which acted as the conductive substrate, a platinum wire acted as the counter electrode, and a silver/silver chloride electrode served as the standard electrode. In order to assess the electrochemical capabilities of the synthesized products, galvanostatic CD (charge–discharge), EIS (electrochemical imped-ance spectroscopy), CV (cyclic voltammetry) and cyclic activity tests were employed. A potential window of 0.10 to 0.70 V and sweeping speeds from 5 to 50 mV s$^{-1}$ were used for the CV measurements. Furthermore, the CV polarization curve was utilized to measure the $C_s$ of the manufactured electrocatalytic product using eqn (3).[32]

$$C_s = \frac{\int_{vc}^{va} I \times dV}{m \times S \times \Delta V} \quad (3)$$

The GCD testing was performed in the 0.1 to 0.7 V range @ 1 to 3 A g$^{-1}$. The GCD analysis was employed to investigate the specific capacitance ($C_s$), energy density ($E_d$) and power density ($P_d$) using eqn (4)–(6), respectively.[33]

$$C_s = \frac{I \times \Delta t}{m \times \Delta V} \quad (4)$$

$$E_d = \frac{C_p \times \Delta V^2}{7.2} \quad (5)$$

$$P_d = \frac{E \times 3600}{\Delta t} \quad (6)$$

The conductive behavior of the electrode material was char-acterized by EIS analysis in the frequency range of 100 Hz to 1000 Hz, and the $R_{ct}$ value was further measured by fitting the data with a Randles circuit. The electrochemical interfacial area of the material was measured by evaluating the electrochemical active surface area (ECSA) in the potential window range from 0.85 to 1.20 V at multiple scan rates. The ECSA polarization curve was employed to measure the value of the electrical double-layer capacitance ($C_{dl}$) according to the following eqn (7).[34]

$$ECSA = \frac{C_{dl}}{C_{sp}} \quad (7)$$

The long-term durability of the electrode material was determined by chronoamperometry measurements @ 0.75 V, and the cyclic testing of the synthesized electrocatalyst.

## 3. Results and discussion

### 3.1. Structural, morphological and textual properties

The crystallinity of the material and phase purity of the SnTe, SnSe and SnTe/SnSe were analyzed with X-ray diffraction at 10 to 80°. Fig. 1 indicates the diffraction peaks of SnTe at 28.43°, 40.94°, 50.3°, 58.52°, 66.04° and 73.0° corresponding to the (200), (220), (202), (400), (420) and (422) indexed planes, respectively, exhibiting the presence of a cubic crystal system, which is consistent with JCPDS: 08-0482. In the case of SnSe, the reflection peaks located at 28.65°, 30.23°, 38.44°, 56.45° and 65.341° attributed to the (201), (111), (311), (122) and (322) planes indicated an orthorhombic crystal system, matching well with JCPDS: 32-1382. In the XRD diffraction pattern of SnTe/SnSe, the existence of the diffraction peaks of both phases clearly indicated the successful synthesis of the nanohybrid materials. The materials formed were highly crystalline, as demonstrated by the low full width at half maximum (FWHM) standards and high peak intensity. Subsequently, a slight shift in the major diffraction peak located at 37.56° to 37.31° was attributed to the variation in the interplanar distance; strain in the crystal lattice was responsible for the generation of vacancies and optimal interaction between the distinct phases in the nanocomposite. The existence of no other peak in the XRD diffractogram showed the purity of the material. The crystallite size of the
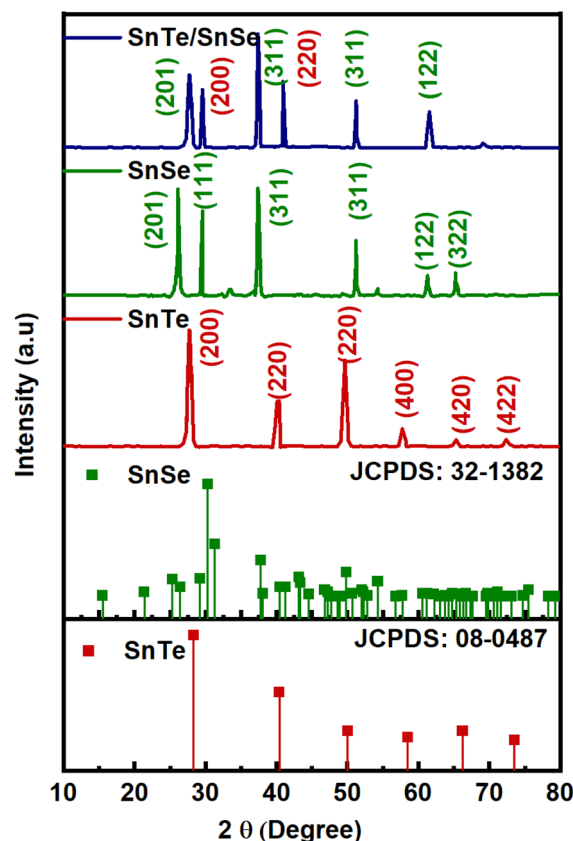


Fig. 1 The XRD diffractograms of SnTe, SnSe and the SnTe/SnSe nanocomposite.

fabricated nanostructured electrode product was determined with the help of eqn (8).[35]

$$D = \frac{K\lambda}{\beta \cos \theta} \qquad (8)$$

Herein, $K$, $\lambda$, $\beta$, $\theta$ and $D$ correspond to the shape factor constant (0.95 for nanosphere particles), X-ray wavelength (Cu-K$\alpha$ = 0.1541 nm), full width at half maximum (FWHM), Bragg's angle and crystallite size, respectively. The crystallite size was measured to be 89, 76 and 53 nm for SnTe, SnSe and SnTe/SnSe, respectively. The smaller crystallite size of the SnTe/SnSe nanoparticles was due to low dislocation density and lattice strain.

FTIR analysis in the 400 to 4000 cm$^{-1}$ region was carried out to check the purity of the produced electrode material. The appearance of a boarder peak at 3000 to 3500 cm$^{-1}$ in all samples was due to the OH$^-$ group of adsorbed water on the interface of the electrocatalytic materials, as shown in Fig. 2(a). However, the slight variation in SnTe/SnSe (STSS) was due to the
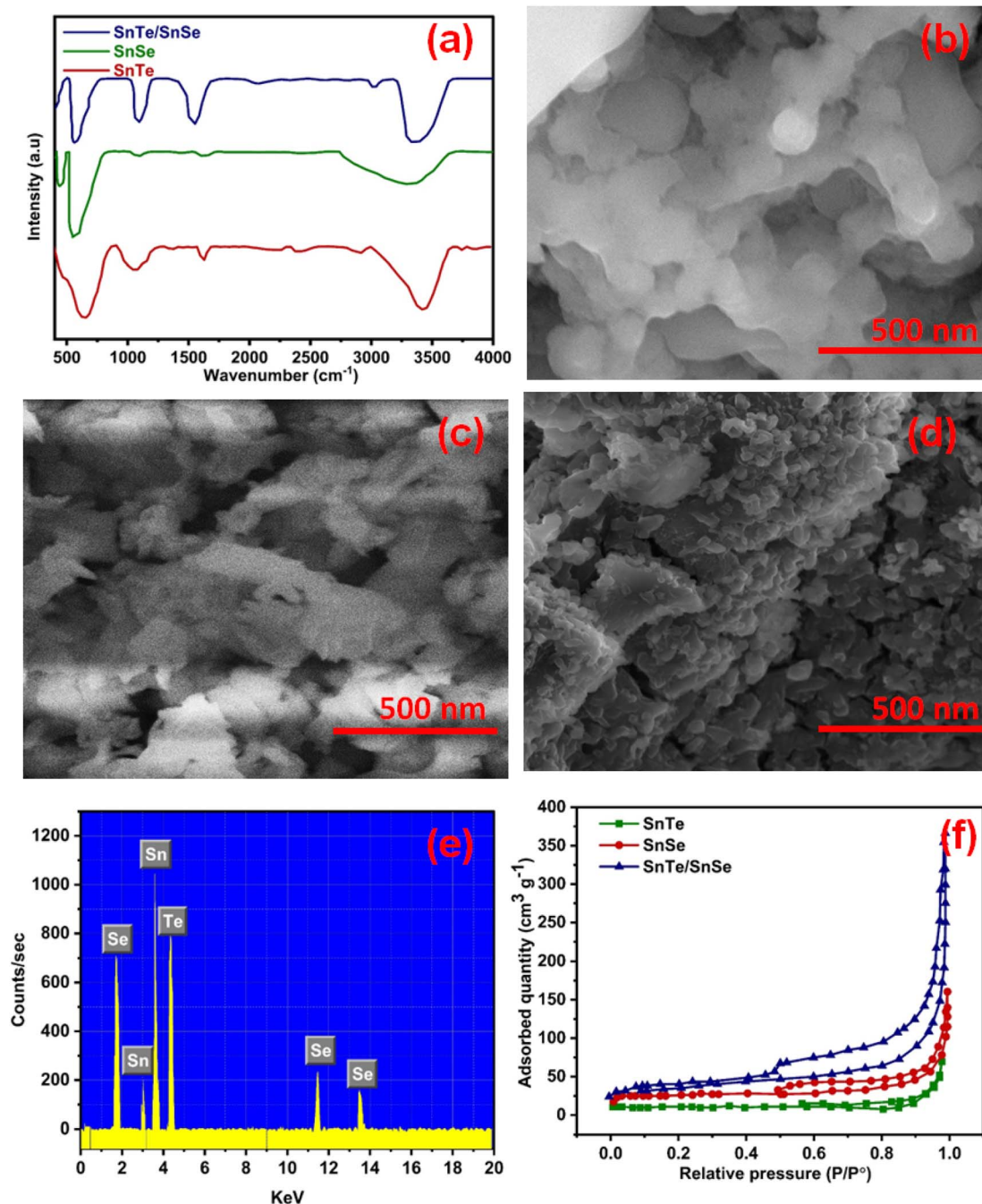


Fig. 2 (a) The FTIR spectra of all synthesized materials; the SEM images of (b) SnTe, (c) SnSe, and (d) SnTe/SnSe; (e) the EDX profile of the SnTe/SnSe nanohybrid; (f) the BET isotherms of SnTe, SnSe and SnT e/SnSe.

incorporation of SnTe into SnSe, which also increased the intensity of the transmittance band. Although the absorption characteristics of the SnTe/SnSe nanocomposites were almost identical, the surface-bound chemical groups had a substantial effect on the Te–Sn–Se bonds in the STSS. The vibration modes that appeared in the range of 400 to 800 cm$^{-1}$ were attributed to metallic interactions with Te and Se. Hence, the presence of all the metallic vibrations of the SnTe and SnSe spectra in the SnTe/SnSe nanocomposite spectrum, and the absence of additional peaks indicate the pureness of the synthesized product, as also confirmed by the XRD analysis.

The surface morphology of SnTe, SnSe and SnTe/SnSe was determined by scanning electron microscopy (SEM), and the results are represented in Fig. 2(b–d). Fig. 2(b) illustrates the morphology of SnTe having agglomerated nanoparticles with irregular geometry. Moreover, SnSe displayed nanosheets having a large surface area, which plays a crucial role in the electrochemical process, as represented in Fig. 2(c). The development of the SnTe/SnSe nanocomposite led to nanoparticle decoration on the nanosheets with a hierarchical morphology, which synergistically enhance the electrochemical characteristics of both SnSe and SnTe in the composite, as shown in Fig. 2(d). Furthermore, the elemental content in the SnTe/SnSe

nanospheres was assessed by EDX, as displayed in Fig. 2(e). The particle sizes of SnTe, SnSe and SnTe/SnSe were 81.26, 65.20 and 51.66 nm, respectively, as calculated with ImageJ software (ImageJ Ver. 1.46r). The surface plots and plot profiles of the fabricated materials are also provided in Fig. S1.† The presence of peaks for Sn, Te and Se in the EDX spectrum indicates composite formation with phase purity. The existence of no other peaks reflects the pureness of the synthesized product, and this result is well in accordance with the FTIR and XRD investigation.

The surface features of the fabricated products were determined by the Brunauer–Emmett–Teller (BET) method based on the analysis of the sorption of N$_2$. The connections between the charged species and the abundance of active sites influence the interfacial area. The BET isotherms displayed the type III loop, indicating the mesoporous surface feature, as shown in Fig. 2(f). Mesoporous structured materials have a huge number of nano-sized catalytic active sites, well-controlled pores, and a large surface area. The surface area of the binary STSS nanocomposite (120 m$^2$ g$^{-1}$) was greater than those of SnTe (25 m$^2$ g$^{-1}$) and SnSe (52 m$^2$ g$^{-1}$). The increased specific surface area (SSA) was due to the combined effect of SnTe and SnSe. The generated binary STSS nanocomposite exhibited a large specific
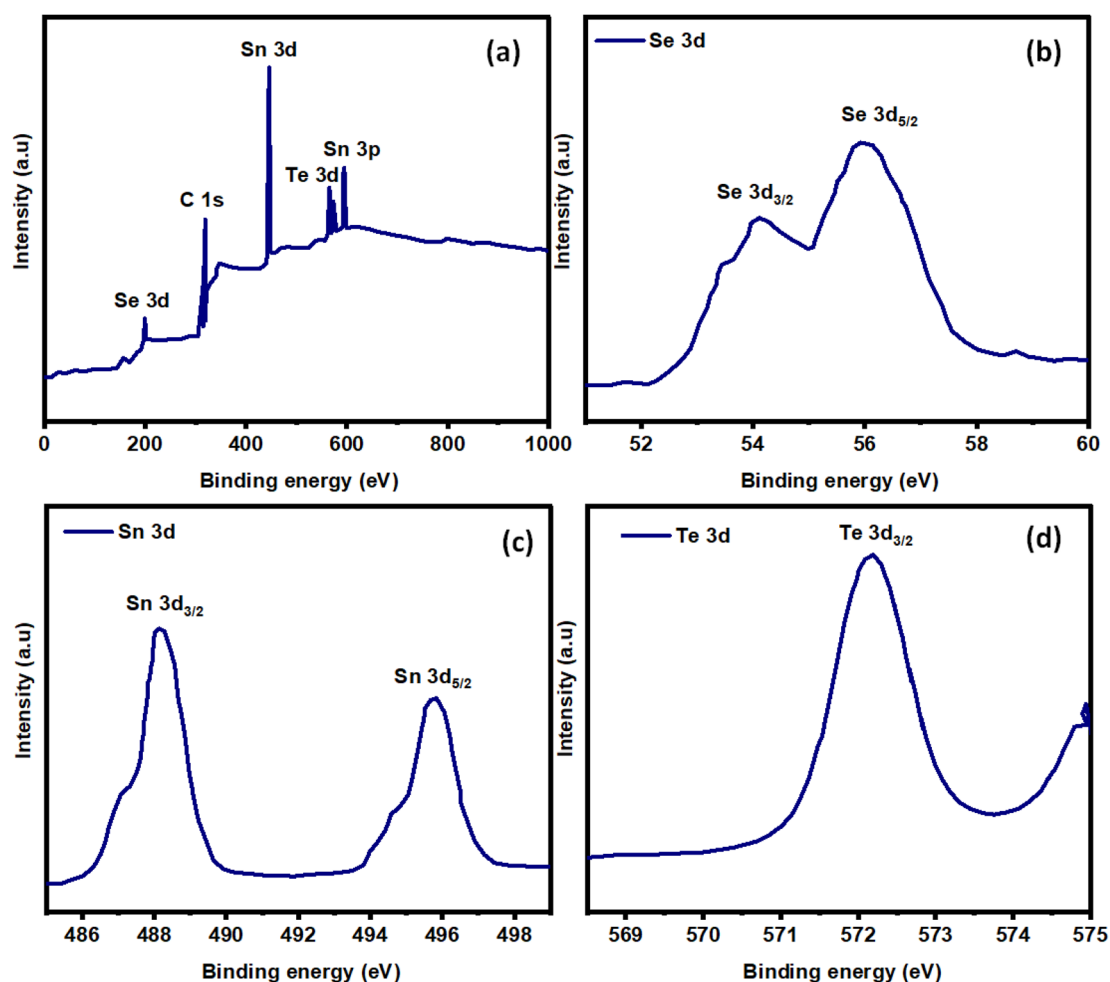


Fig. 3 The XPS spectra in the (a) full-width scan range and the (b) Se 3d, (c) Sn 3d and (d) Te 3d regions.
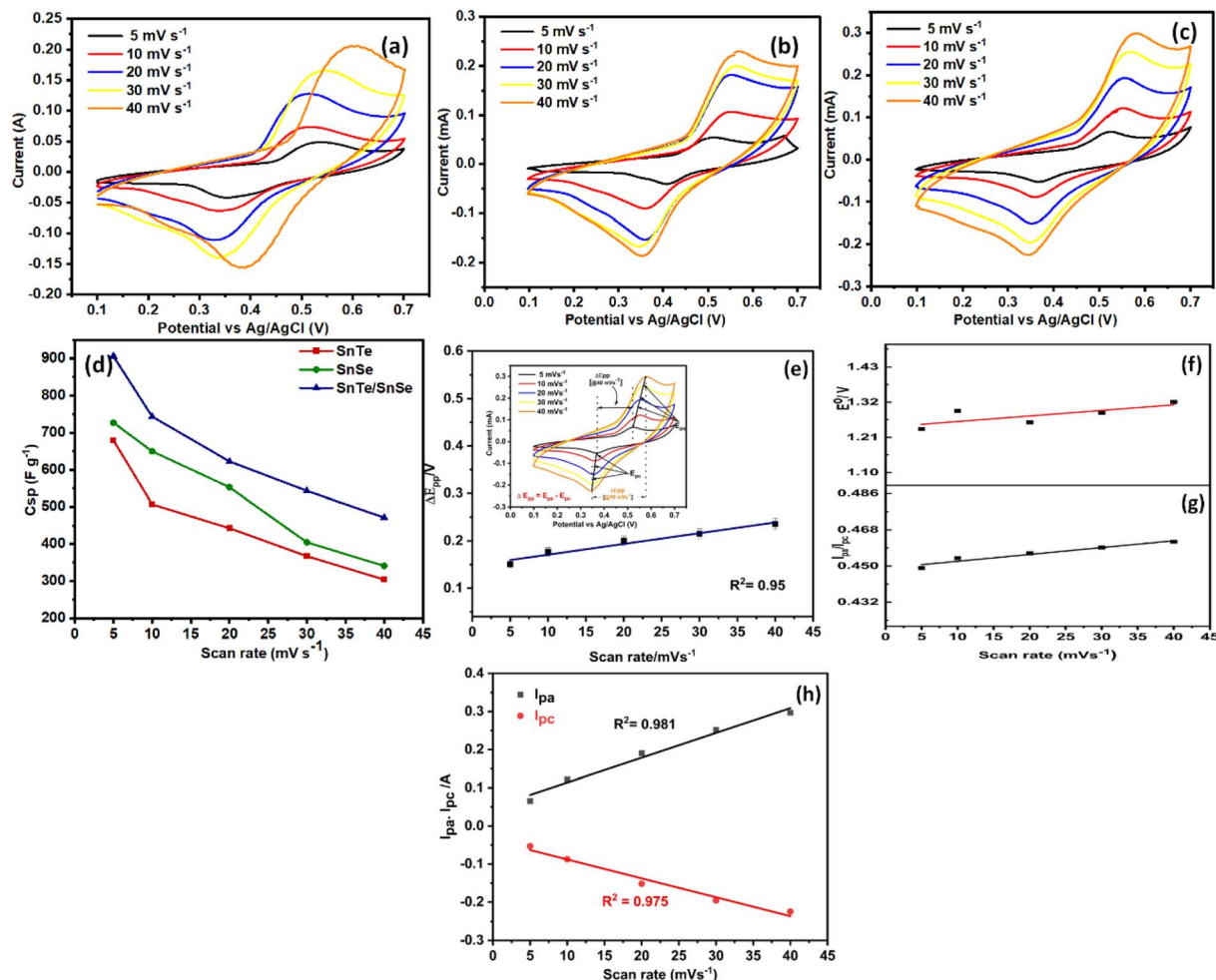
Fig. 4 The CVs of (a) SnTe, (b) SnSe, and (c) SnTe/SnSe; (d) The plot between $C_s$ vs. sweeping speed; (e) Peak potential difference vs. scan rate of the STSS; (f) formal potential ($E^0$), (g) peak anodic/peak cathodic currents ($I_{pa}/I_{pc}$) vs. scan rate, and (h) the variations in peak cathodic and peak anodic currents against the scan rate.

exposed area and mesoporous assembly, implying that the interface of the composite and the charged electrolyte species may come in close contact during the electrocatalytic process.

The XPS technique was utilized to analyze the valence state of the fabricated products. The full width scan spectra indicated the presence of Sn, Te and Se elements, as presented in Fig. 3(a). The presence of two XPS bands at 54.4 and 56.4 eV belonging to Se $3d_{3/2}$ and Se $3d_{5/2}$ suggests that Se existed in the −2 valence state, as shown in Fig. 3(b). The existence of two deconvoluted bands at 496 and 488 eV, which could be attributed to Sn $3d_{5/2}$ and Sn $3d_{3/2}$, respectively, indicate that the tin existed in the +2 valence state, as represented in Fig. 3(c). Furthermore, the presence of the Te $3d_{3/2}$ peak at 572.5 eV confirms the existence of tellurium in the −2 state. The XPS results reveal that Sn, Se and Te exhibited the +2, −2 and −2 valence states, respectively.

### 3.2. Electrochemical study

The electrochemical efficiency of the SnTe, SnSe and SnTe/SnSe materials was measured using a potentiostat configured in a 3-electrode system in 2.0 M KOH. The CV analysis

was performed at a sweeping speed of 5–40 mV s$^{-1}$, and the potential window ranged from 0.1 to 0.7 V, as represented in Fig. 4(a–c). The CV polarization plots of all synthesized materials displayed quasi-symmetrical peaks, and the presence of prominent oxidation and reduction peaks attributed to the electrochemical reaction suggested the pseudocapacitive behavior of the materials.

The CV polarization curves were further used to measure the $C_s$ of SnTe, SnSe and STSS with the help of eqn (4). The SnTe, SnSe and SSTS displayed $C_s$ values of 560.39, 726.83, and 905 F g$^{-1}$ at a sweeping degree of 5 mV s$^{-1}$, as displayed in Fig. 4(a–c). These findings manifest that the STSS nanocomposite had the highest $C_s$ value may be due to the synergy between the interaction of Se and Te with the Sn ions and the spherical morphology, which may offer less resistance and provide short paths for ionic diffusion and transportation.[36] Additionally, when the sweep rate was enhanced, the $C_s$ of the materials decreased with respect to the scanning speed, respectively, as seen in Fig. 4(d). This may be attributed to the less opportunity for ionic interactions with the electrode surface and the

inability to penetrate the surface at larger sweeping rates. Furthermore, the oxidation and reduction peaks of every material shifted to higher and lower potentials, respectively, as the sweeping speed was increased from 5 to 40 mV s$^{-1}$. Both peak current magnitudes and the region underneath the voltammograms increased with the rise in sweeping speed, as represented in Fig. 4(e). However, the diffusion effect was determined based on the peak-to-peak separation potential, formal potential and the proportion of the cathodic peak current to the anodic peak current and was computed using the following expressions, respectively.[35]

$$\Delta E_{pp} = E_{pa} - E_{pc} \tag{9}$$

$$E^0 = \frac{E_{pa} + E_{pc}}{2} \approx 0.29V \tag{10}$$

$$\frac{I_{Pa}}{I_{pc}} \approx -1.13 \tag{11}$$

where $E_{pp}$, $E_{pc}$, $E_{pa}$, $E^0$, $I_{pc}$ and $I_{pa}$ correspond to the peak-to-peak potential, reduction peak potential, anodic potential, formal potential, cathodic peak current and oxidation peak current, respectively. All the cyclic voltammograms revealed
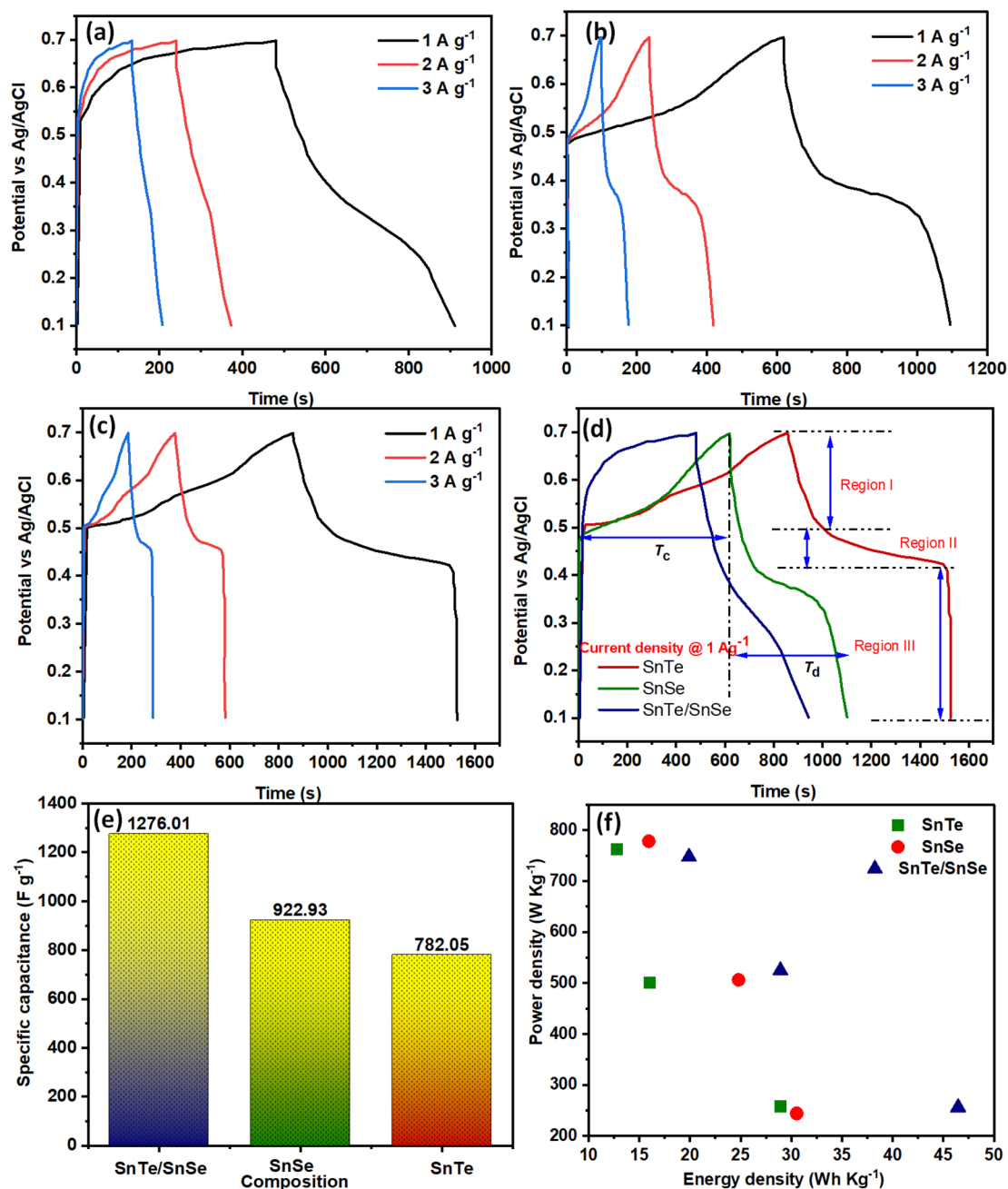


Fig. 5  The GCD plot profiles of (a) SnTe, (b) SnSe, (c) SnTe/SnSe; (d) the plot profiles of $C_s$ vs. material composition; (e) comparison between the GCD plots @ 1 Ag$^{-1}$; (f) the Roenge plot profile of the SnTe/SnSe nanohybrid.

that the STSS nanocomposite exhibited a semi-symmetrical reversible process. The peak potentials of the fabricated materials rose with the rise in scan speed, as represented in Fig. 4(e).[37] Furthermore, the ratio $I_{pa}/I_{pc}$ showed a linear correlation with the sweeping speed, as represented by Fig. 4(f–g). As demonstrated in Fig. 4(h), $I_{pa}$ and $I_{pc}$ exhibited a linear plot with the sweeping speed, and the anodic peak current increased and the reduction peak currents decreased with the increase in sweeping speed. The CV analysis revealed that the reduction peak shifted toward the lower potential region and the oxidation peak moved toward higher potentials with rising sweeping speed for all materials, and the $C_s$ of the synthesized products reduced with a rising scan rate.

The charge–discharge behavior of SnTe, SnSe and SnTe/SnSe was measured by galvanostatic charge–discharge (GCD) analysis at 1.0–3.0 A g$^{-1}$, as represented in Fig. 5(a–c), respectively. The semi-symmetrical and non-linear trend of the GCD polarization curves of all fabricated samples revealed the pseudocapacitive nature of the materials. However, the STSS displayed a GCD polarization curve with a greater non-linear trend than the other pristine materials, showing remarkable pseudocapacitor behavior, greater reversibility of the redox reaction and greater discharge time. Fig. 5(d) displays the comparison of the charge–discharge plot profiles of SnTe, SnSe and SnTe/SnSe, and all discharge curves display 3 distinct regions: region I (0.69–0.49 V for the IR drop), region II (0.49–0.41 for EDLC characteristics) and region III (0.41–0.1 V for pseudocapacitor characteristics). However, the greater potential value of region III (0.21 V) than region II (0.08 V) also confirms the pseudocapacitive activity of the electrode materials, and the comparison between the GCD polarization curves of the different electrode materials at 1 A g$^{-1}$ is displayed in Fig. 5(e). The $C_s$ of the synthesized electrode materials were estimated using eqn (4), and the calculated $C_s$ values indicate that the binary nanocomposite (1276 F g$^{-1}$) had greater $C_s$ than SnSe (922.93 F g$^{-1}$) and SnTe (782.05 F g$^{-1}$) at 1 A g$^{-1}$, as represented in Fig. 4(e). Moreover, the calculated $E_d$ values were 46.45, 30.52, 28.92 W h kg$^{-1}$ and the $P_d$ values were 256, 244, and 258 W kg$^{-1}$ for STSS, SnSe and SnTe, respectively. A comparison between the fabricated electrodes is given in Table 1. The correlation between the power density and $E_d$ is expressed in the Roenge

plots displayed in Fig. 5(f). The irregular spherical morphology of the material has a great impact on the GCD analysis and is responsible for the higher $C_s$, $E_d$, and $P_d$ values of the composite than those of the pristine materials, thus making the nanocomposite a suitable candidate for supercapacitor applications.[38] Additionally, as the current density was increased from 1 to 3 A g$^{-1}$, the specific power, $C_s$ and $E_d$ of the generated products decreased, which may be because the ion/proton concentration at a relatively fast scan rate significantly prevents charge transport into the electrode region during the power storage phase, as seen in Fig. 4(e).

The ECSA investigation was employed to measure the double-layer capacitance ($C_{dl}$) of the prepared electrode in the non-faradaic region across a small potential range (0.85–1.20 V against RHE), as represented in Fig. 6(a–c). The $C_{dl}$ was computed by plotting a graph between the current density and scanning rates from 10-50 mV s$^{-1}$, as presented in Fig. 6(d–e). The results of $C_{dl}$ indicated that the STSS (31.28 mF) exhibited a larger $C_{dl}$ value than those of SnTe (23.22 mF) and SnSe (26.35 mF). Further, the $C_{dl}$ values and eqn (7) were employed to compute the ECSA of STSS, SnTe and SnSe, which were found to be 783.5, 580.5 and 658.5 cm$^2$, respectively. The higher electrochemical surface area of the STSS is due to the small crystallite size and the synergetic behavior of Se and Te with Sn. The electrode material with a greater $C_{dl}$ value offers a great number of active regions for adsorption, as well as efficient charge transformation, resulting in high electrocatalytic efficiency.

The electroconductivity of the fabricated electrode substances was determined using electrochemical impedance spectroscopy (EIS) analysis in the 100 Hz to 100 kHz frequency range. Charge transfer resistance ($R_{ct}$), was estimated using the diameter of the small semi-circle, and ion diffusion was estimated using the slope of the line, as shown in Fig. 6(a). The small semi-circles appeared in the high-frequency region and displayed the $R_{ct}$ values of the fabricated materials. The Nyquist plot profile displayed a smaller $R_{ct}$ value for STSS (0.89 Ω) than those of SnSe (1.13 Ω) and SnTe (1.97 Ω). The slope line of the EIS plot of the STSS was more directed toward 45°, indicating the faster diffusion of the KOH ions at the interface of the electrocatalytic materials.[38] The small $R_{ct}$ value and faster diffusion of the electrolyte ion indicate that the STSS has greater

**Table 1** Comparative analysis of fabricated STSS electrode with other reported electrodes for supercapacitor application

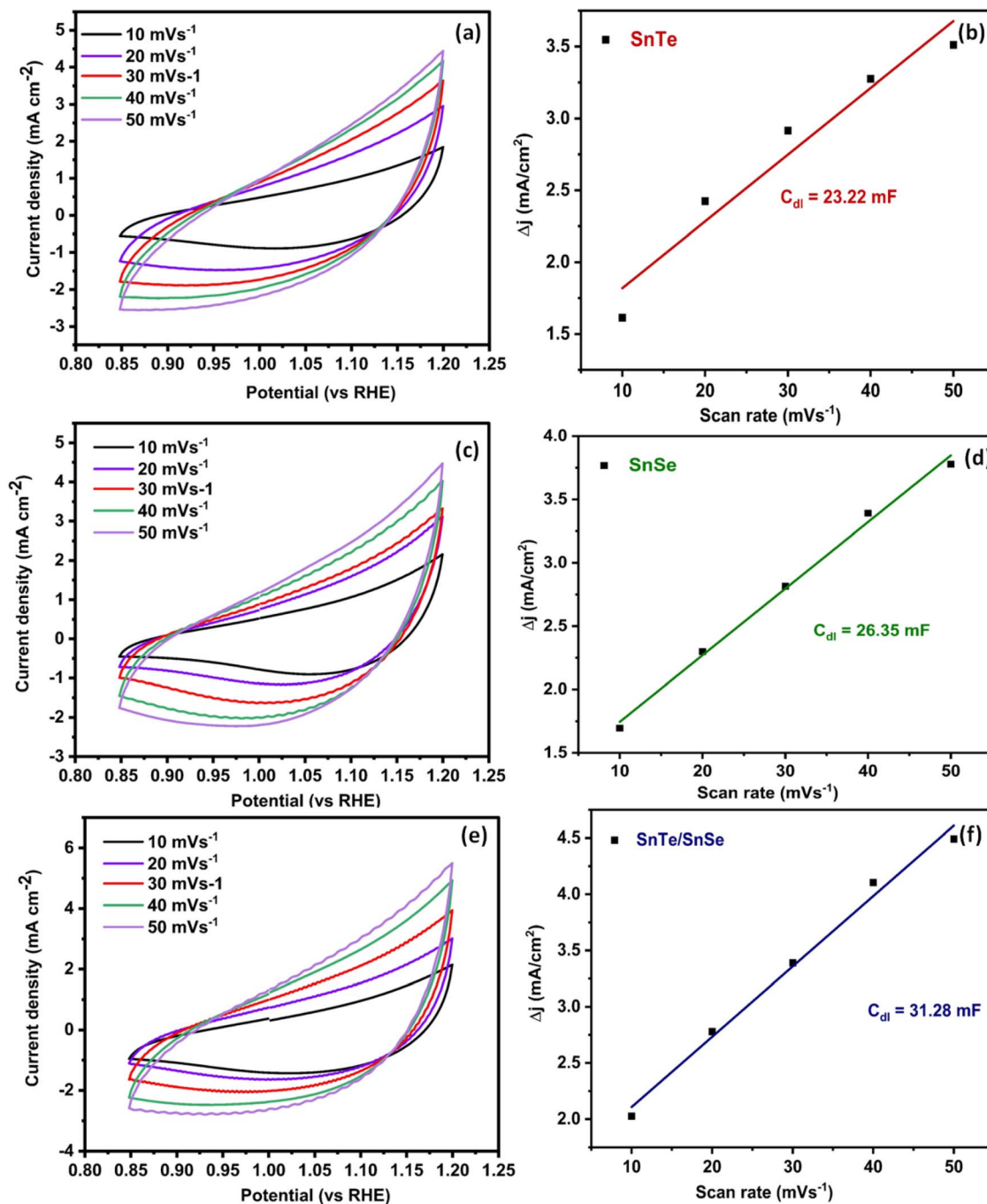| Sr no. | Material | Substrate | Electrolyte | Specific capacitance (F g$^{-1}$) | Current density (A g$^{-1}$) | Ref. |
|--------|----------|-----------|-------------|-----------------------------------|------------------------------|------|
| 1 | NiS$_2$/RGO | Ni foam (NF) | KOH | 722 | 1 | 38 |
| 2 | NiS$_2$/MoS$_2$ | NF | KOH | 446 | 5 | 39 |
| 3 | NiS/NiTe/N | NF | KOH | 969.14 | 17.8 | 40 |
| 4 | CuO/NiO | NF | Na$_2$SO$_4$ | 35.63 | 0.3 | 41 |
| 5 | TiO$_2$/CuSe | NF | KOH | 40.5 | 1.0 | 42 |
| 6 | WS$_2$ | Carbon fiber | KOH | 399 | 1.0 | 43 |
| 7 | CuCo$_2$O$_4$/MnS | NF | KOH | 345 | 1.0 | 44 |
| 8 | CoNi$_2$S$_4$ | Carbon cloth | KOH | 1165 | 1 | 45 |
| 9 | CoSe$_2$ | Carbon fiber | KOH | 713 | 1 | 46 |
| 10 | Ni$_3$S$_2$/GNS | Carbon fiber | KOH | 1420 | 2 | 47 |
| 11 | SnTe/SnSe | NF | KOH | 1276 | 1 | Present work |

Fig. 6 (a–c) The ECSA of SnTe, SnSe and SnTe/SnSe and (d and e) the $C_{dl}$ of SnTe, SnSe and SnTe/SnSe.

electrochemical conductivity and a faster charging rate than the other fabricated materials.

The mechanical stability of the STSS nanohybrid electrode was investigated by chronoamperometry, as represented in Fig. 7(b). The chronoamperometry result suggested that the nanohybrid was stable over 50 h at 0.75 V (V vs. Ag/AgCl), which is much better than that of $RuO_2$ used as a benchmark. The GCD stability of the STSS nanohybrid materials (0.005 g) was determined over 5000 cycles, as represented in Fig. 7(c). The STSS displayed a rate capability of 98.04% over the first 2500

cycles and also 96.08% capacitance retention at the 5000th cycle. Fig. 7(d) shows the cyclic stability based on the CV analysis of the nanohybrid materials over 5000 cycles. The voltammograms of the fabricated materials exhibited a very small change in current after the stability test. The minor change in the efficiency of the nanohybrid materials was owing to charge deposition at the interface of the electrocatalytic species, blockage of the active sites and the destruction of the active zone. Furthermore, the structural stability of the materials was investigated by XRD analysis, and their diffractograms
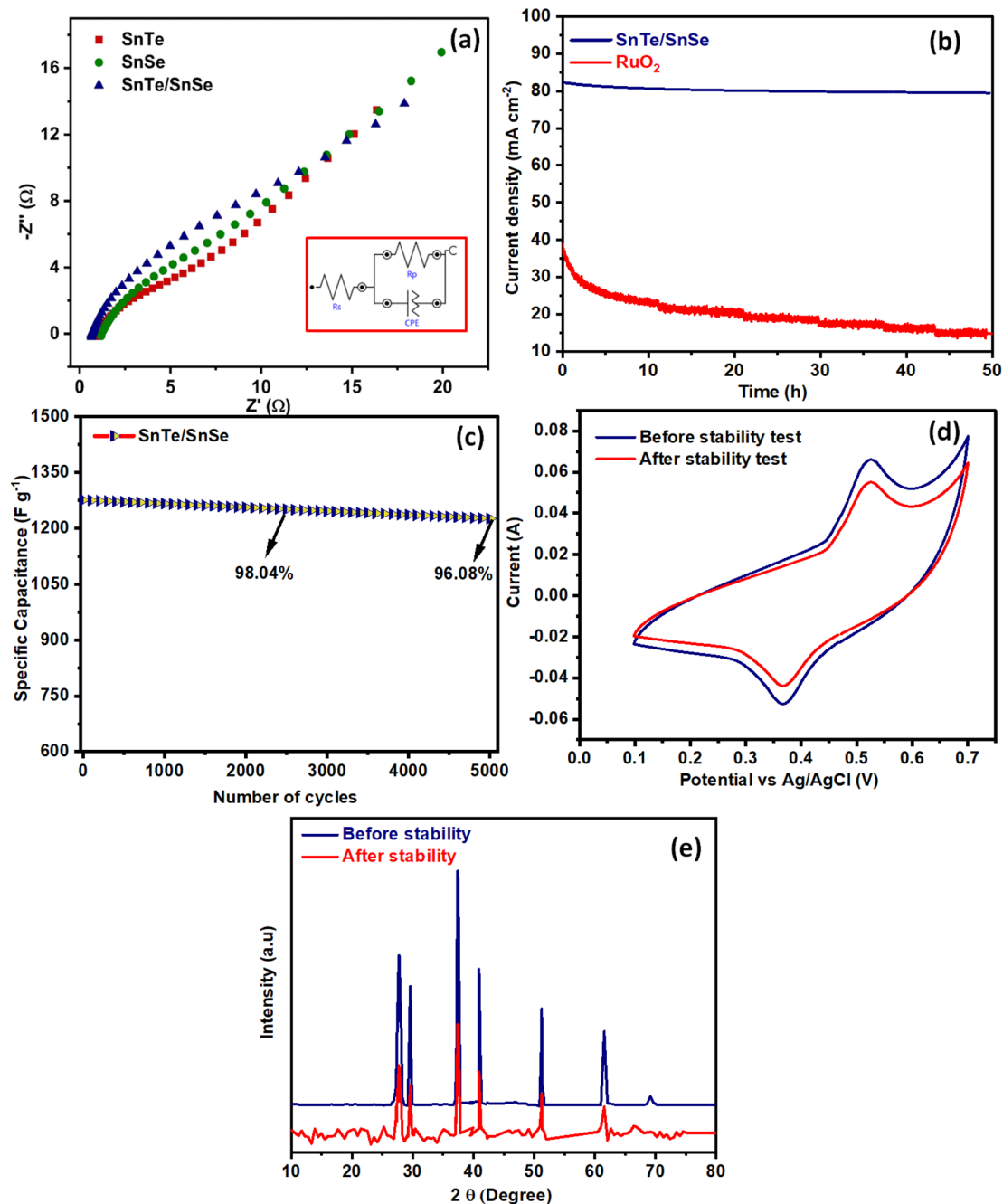
**Fig. 7** (a) The EIS plot profiles of SnTe, SnSe and SnTe/SnSe; (b) the chronoamperometry profile of the STSS; (c) the graph of specific capacitance *vs.* the number of cycles for STSS; (d) the cycling stability of the STSS and (e) the XRD diffractogram of the STSS nanohybrid.

represented that the structures remained the same, with a small change in the intensity due to the coverage of the active sites of the electrocatalyst with charge accumulation and $OH^-$ ions, as represented in Fig. 7(e).

## 4. The two-electrode system

The practical applicability of the STSS nanohybrid was evaluated with a system containing two symmetric electrodes in the presence of 2.0 M KOH. The potential capability of the STSS nanohybrid was observed by employing different electrochemical tests, such as CV, GCD and EIS analysis. Fig. 8(a) illustrates the CV investigation of the STSS nanohybrid, which displays a reversible faradaic redox process. The CV analysis was further used to investigate the $C_s$ of the STSS nanohybrid using eqn (3) and obtained the $C_s$ was 426.39 F g$^{-1}$ @ 5 mV s$^{-1}$. The $C_s$ of the STSS decreased with an increase in sweeping speed because the $OH^-$ ions have limited time for penetration at the interface of the electrocatalytic species. The $C_s$ of the STSS nanohybrid was investigated using the GCD plot profiles at 1, 2
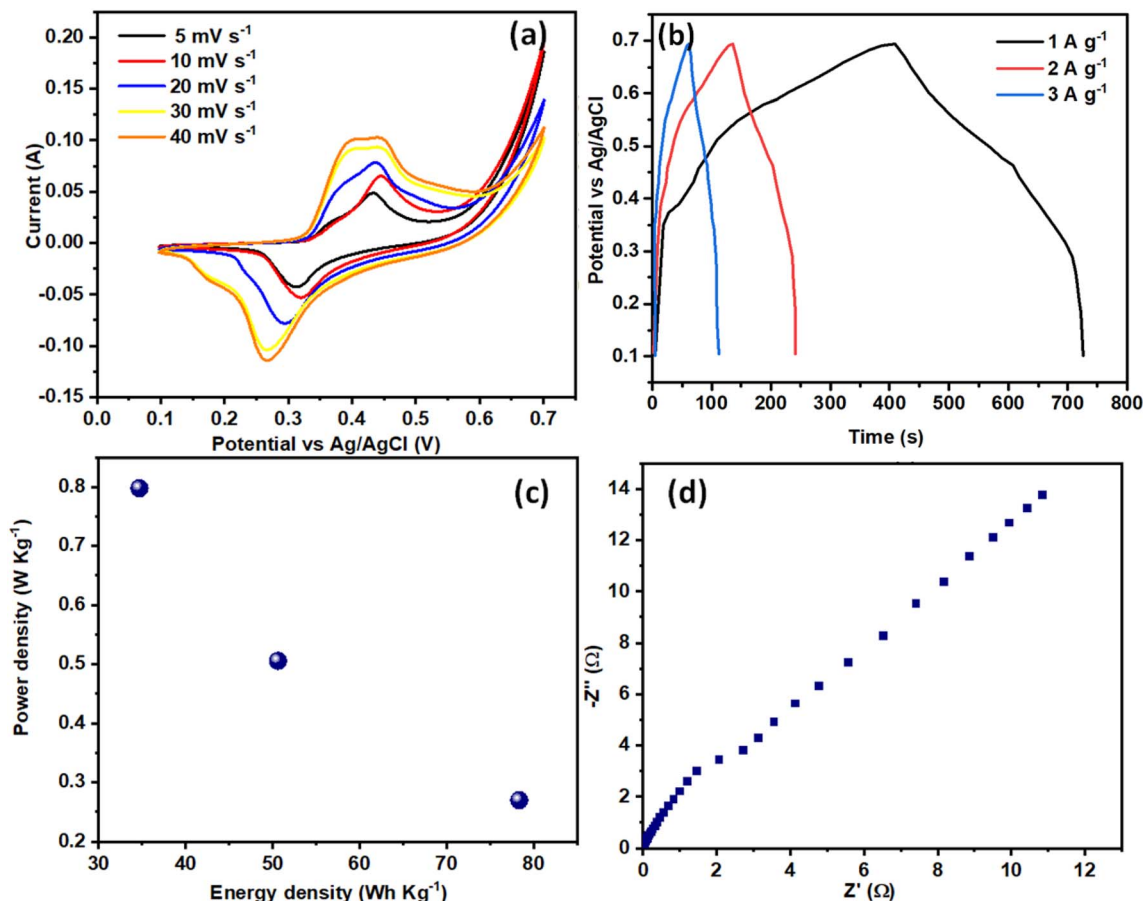
**Fig. 8** (a) The cyclic voltammograms of STSS, (b) GCD analysis of STSS, (c) Roenge plot of STSS and (d) EIS spectra of the STSS nanohybrid with a two-electrode system.

and 3 A g$^{-1}$. The $C_s$ values of the STSS calculated with eqn (4) were 537.22, 395.26 and 245.13 F g$^{-1}$ at 1, 2 and 3 A g$^{-1}$, respectively. The $E_d$ values of 78.32, 50.6 and 34.68 W h kg$^{-1}$ and $P_d$ values of 0.27, 0.50 and 0.79 W kg$^{-1}$ were obtained at 1, 2 and 3 A g$^{-1}$ using eqn (12) and (13), respectively. The correlation between $E_d$ and $P_d$ is expressed in Fig. 8(c). The EIS plot profile of the STSS nanohybrid displayed a larger $R_{ct}$ value of 2.3 Ω than the three-electrode system.

$$E_d = \frac{1}{2}C_s(V)^2 \quad (12)$$

$$P_d = \frac{E_d}{t} \quad (13)$$

Compared with the two-electrode system, the three-electrode system showed superior electrochemical efficiency. Since the electrode material is exposed to an excessive amount of the electrolyte solution, the mobile ions involved in the charge storage process have unfettered access to the electrode material, resulting in a very high $C_s$ response. Unfortunately, the three-electrode cell design is not useful in real-time practice, and commercial supercapacitors are made using a two-electrode structure. Supercapacitors may be mass-produced at minimal

cost because of the utilization of a two-electrode configuration, which reduces the electrolyte ions required for operation. The greater electrochemical efficiency can be ascribed to several factors, such as the synergistic effects of the two highly capacitive electrode materials, the remarkable ionic transport medium, and the greater number of active sites on the surface area provided by the nanostructure of STSS.

## 5. Conclusion

In this work, hierarchical nanoparticles were developed using a hydrothermal strategy for supercapacitors. Several analytical tools were utilized to assess the specific surface area (SSA), structure, and textural properties of the fabricated product. The electroanalytical analysis was performed with three- and two-electrode systems in 2.0 M KOH. The electrocatalytic result suggests that the STSS nanohybrid shows an outstanding $C_s$ of 1276 F g$^{-1}$, an $E_d$ of 46.45 W h kg$^{-1}$ and a $P_d$ of 256 W kg$^{-1}$ at 1 Ag$^{-1}$. Among the fabricated electrodes, the STSS displayed the highest $C_{dl}$ value (31.28 mF). However, the stability results indicate that the fabricated materials show stable behavior with a retention capacitance of 96% over 50 h and excellent structural stability over 5000 cycles, as evidenced by XRD analysis. The practical application of the STSS

nanohybrid was investigated with a two-electrode system having a $C_s$ of 537.72 F g$^{-1}$ and an $E_d$ of 78.32 W h kg$^{-1}$. This research not only presents the possibility of constructing electrodes from diverse composite-type materials, but also proposes a potential way to investigate the reaction processes of different energy-storage materials.

## Conflicts of interest

There are no conflicts to declare.

## Acknowledgements

## References

1 J. N. Shaturaev and J. Shaturaev, *Indonesian J. Educ. Res. Rev.*, 2023, **3**, 51–58.

2 S. Wang, T. Li, Y. Yin, N. Chang, H. Zhang and X. Li, *Nano Energy*, 2022, **96**, 107120.

3 S. Q. Liew and H. K. Jun, *Nanostructured Materials for Supercapacitors*, 2022, pp. 71–100.

4 U. Latif, M. A. Raza, Z. U. Rehman, J. Iqbal, N. Lee, S. M. Z. Mehdi, M. F. Maqsood and S. Hussain, *Int. J. Energy Res.*, 2022, **46**, 9643–9666.

5 K. Yang, L. Hu, Y. Wang, J. Xia, M. Sun, Y. Zhang, C. Gou and C. Jia, *J. Mater. Chem. A*, 2022, **10**, 12532–12543.

6 M. K. Song, S. Cheng, H. Chen, W. Qin, K. W. Nam, S. Xu, X. Q. Yang, A. Bongiorno, J. Lee, J. Bai, T. A. Tyson, J. Cho and M. Liu, *Nano Lett.*, 2012, **12**, 3483–3490.

7 L. Chai, P. Wang, X. Liu, Y. Sun, X. Li and J. Pan, *J. Power Sources*, 2022, **532**, 231324.

8 R. Miao, C. Sun, J. Li, Y. Sun, Y. Chen, J. Pan, Y. Tang and P. Wan, *Dalton Trans.*, 2022, **51**, 18213–18223.

9 S. Wang, S. Lu, W. Xu, S. Li, J. Meng and Y. Xin, *New J. Chem.*, 2022, **46**, 12184–12195.

10 S. B. Aziz, R. T. Abdulwahid, M. F. Z. Kadir, H. O. Ghareeb, T. Ahamad and S. M. Alshehri, *J. Ind. Eng. Chem.*, 2022, **105**, 414–426.

11 S. A. Ahmad, M. Z. U. Shah, M. Arif, E. Ullah, S. ur Rahman, M. S. U. Shah, S. M. Eldin, P. Song, M. Sajjad and A. Shah, *Ceram. Int.*, DOI: **10.1016/J.CERAMINT.2023.03.122**.

12 H. Peçenek, S. Yetiman, F. K. Dokan, M. S. Onses, E. Yılmaz and E. Sahmetlioglu, *Ceram. Int.*, 2022, **48**, 7253–7260.

13 S. Vijayakumar, S. Nagamuthu and G. Muralidharan, *ACS Appl. Mater. Interfaces*, 2013, **5**, 2188–2196.

14 D. Yu, X. Zhong, D. Liu and Y. Liang, *RSC Adv.*, 2019, **9**, 32232–32239.

15 S. Rada, M. Unguresan, M. Rada, D. Cuibus, J. Zhang, A. Pengfei, R. Suciu, A. Bot and E. Culea, *J. Electrochem. Soc.*, 2019, **166**, A3987–A3996.

16 Q. Meng, K. Cai, Y. Chen and L. Chen, *Nano Energy*, 2017, **36**, 268–285.

17 L. Hao, X. Li and L. Zhi, *Adv. Mater.*, 2013, **25**, 3899–3904.

18 S. P. Lim, N. M. Huang and H. N. Lim, *Ceram. Int.*, 2013, **39**, 6647–6655.

19 B. Kirubasankar, V. Murugadoss, J. Lin, T. Ding, M. Dong, H. Liu, J. Zhang, T. Li, N. Wang, Z. Guo and S. Angaiah, *Nanoscale*, 2018, **10**, 20414–20425.

20 S. Zhang, D. Yang, M. Zhang, Y. Liu, T. Xu, J. Yang and Z. Z. Yu, *Inorg. Chem. Front.*, 2020, **7**, 477–486.

21 X. Wei, X. Wang, X. Tan, Q. An and L. Mai, *Adv. Funct. Mater.*, 2018, **28**, 1804458.

22 B. Pandit, C. D. Jadhav, P. G. Chavan, H. S. Tarkas, J. V. Sali, R. B. Gupta and B. R. Sankapal, *IEEE Trans. Power Electron.*, 2020, **35**, 11344–11351.

23 S. Y. Ahmed, S. G. Mohamed, S. Y. Attia, Y. F. Barakat, M. A. Shoeib and N. S. Tantawy, *J. Electroanal. Chem.*, 2021, **883**, 115063.

24 D. Ni, Y. Chen, X. Yang, C. Liu and K. Cai, *J. Alloys Compd.*, 2018, **737**, 623–629.

25 B. Ye, X. Cao, Q. Zhao and J. Wang, *J. Phys. Chem. C*, 2020, **124**, 21242–21249.

26 B. Ye, M. Huang, Q. Bao, S. Jiang, J. Ge, H. Zhao, L. Fan, J. Lin and J. Wu, *ChemElectroChem*, 2018, **5**, 507–514.

27 C. Xu, J. Kang, Y. Zhao, L. Zhu, J. Zhang, B. Wei and H. Wang, *New J. Chem.*, 2023, **47**, 3159–3166.

28 A. M. Zardkhoshoui and S. S. H. Davarani, *J. Colloid Interface Sci.*, 2019, **535**, 195–204.

29 S. Arunpandiyan, A. Raja, S. Bharathi and A. Arivarasan, *J. Alloys Compd.*, 2021, **883**, 160791.

30 Y. Tian, Y. Ruan, J. Zhang, Z. Yang, J. Jiang and C. Wang, *Electrochim. Acta*, 2017, **250**, 327–334.

31 J. Zheng, K. Cheng, R. Zhang, Y. Wu, Y. Yang and P. Yu, *J. Mater. Sci.: Mater. Electron.*, 2020, **31**, 9366–9376.

32 N. Bibi, I. Ahmad, M. Mubeen, M. N. Ashiq, S. Zhang and A. Iqbal, *J. Energy Storage*, 2021, **37**, 102505.

33 N. Bibi, M. Z. Hussain, S. Hussain, S. Ahmed, I. Ahmad, S. Zhang and A. Iqbal, *Appl. Surf. Sci.*, 2019, **495**, 143587.

34 Q. Wang, H. Wang, S. Qi, Z. Su, K. Chen, X. Yu, A. Xie and S. Luo, *J. Electrochem. Soc.*, 2022, **169**, 026508.

35 M. K. Khan, S. A. Tahir, A. Ashfaq, A. Ali, W. Ahmad, M. Haneef, S. Mushtaq, R. Saeed, K. M. Khan and K. shabbir, *Opt. Mater.*, 2022, **128**, 112406.

36 C. Y. Foo, A. Sumboja, D. J. H. Tan, J. Wang and P. S. Lee, *Adv. Energy Mater.*, 2014, **4**, 1400236.

37 Q. Yang, F. Mo, Z. Liu, L. Ma, X. Li, D. Fang, S. Chen, S. Zhang and C. Zhi, *Adv. Mater.*, 2019, **31**, 1901521.

38 H. Cui, G. Zhu, X. Liu, F. Liu, Y. Xie, C. Yang, T. Lin, H. Gu, F. Huang, H. Cui, G. Zhu, F. Liu, Y. Xie, C. Yang, T. Lin, H. Gu, F. Huang and X. Liu, *Adv. Sci.*, 2015, **2**, 1500126.

39 Y. Liu, J. Sun, S. Lin, Z. Xu and L. Li, *J. Alloys Compd.*, 2020, **820**, 153113.

40 S. Chen, B. Wu, H. Qian, Z. Wu, P. Liu, F. Li, H. He, J. Wu and B. Liu, *J. Power Sources*, 2019, **438**, 227000.

41 S. Chatterjee, A. Ray, M. Mandal, S. Das and S. K. Bhattacharya, *J. Mater. Eng. Perform.*, 2020, **29**, 8036–8048.

**RSC Advances**

**Paper**

42 M. Z. Ullah Shah, M. S. Javed, M. Sajjad, A. Shah, M. S. Shah, S. ur Rahman, A. Mahmood, M. A. Ahmad, M. A. Assiri and H. Hou, *J. Sci.: Adv. Mater. Devices*, 2022, **7**, 100418.

43 X. Shang, J. Q. Chi, S. S. Lu, J. X. Gou, B. Dong, X. Li, Y. R. Liu, K. L. Yan, Y. M. Chai and C. G. Liu, *Appl. Surf. Sci.*, 2017, **392**, 708–714.

44 Z. K. Heiba, M. A. Deyab, N. M. Farag, M. B. Mohamed and S. I. Ahmed, *J. Sol-Gel Sci. Technol.*, 2022, **2022**, 1–10.

45 P. Liu, Y. Sui, F. Wei, J. Qi, Q. Meng, Y. Ren and Y. He, *J. Mater. Sci.: Mater. Electron.*, 2019, **30**(21), 19077–19086.

46 K. Krishnamoorthy, G. K. Veerasubramani, S. Radhakrishnan and S. J. Kim, *Chem. Eng. J.*, 2014, **251**, 116–122.

47 Z. Zhang, X. Liu, X. Qi, Z. Huang, L. Ren and J. Zhong, *RSC Adv.*, 2014, **4**, 37278–37283.